



## Microstructural characterization of in situ synthesized TiB in cast Ti-1100–0.10B alloy

Bin-guo FU, Hong-wei WANG, Chun-ming ZOU, Zun-jie WEI

National Key Laboratory for Precision Heat Processing of Metals, Harbin Institute of Technology, Harbin 150001, China

Received 26 August 2014; accepted 28 December 2014

**Abstract:** The as-cast Ti-1100–0.10B alloy was prepared by a vacuum induction-melting technology. The microstructural characterization of in situ synthesized TiB and the interfacial structure of TiB/Ti matrix were systematically investigated. The results demonstrate that the TiB phase precipitates preferably at the prior  $\beta$  grain boundaries. The TiB phase grows along [010] direction with a typical needle-like morphology. The transversal section of TiB is hexagonal, and the interfaces between TiB and the Ti matrix are clean without precipitation phase. The stacking faults are observed on the (100) plane of the TiB phase, which are ascribed to the locations of boron (B) atoms in the crystal structure of TiB and the lattice mismatch energy between TiB and Ti matrix.

**Key words:** Ti alloy; casting; microstructure; TiB

### 1 Introduction

High temperature Ti alloys are widely used in aerospace engines due to the combination of excellent properties, such as high specific strength and ability to withstand elevated temperatures up to 600 °C [1–3]. In recently, boron (B)-modified Ti alloys containing B less than 1.5% (mass fraction) have attracted considerable interest because of the increased strength, stiffness, fatigue resistance and wear resistance as compared with the matrix alloys [4, 5]. The addition of B to Ti alloys may precipitate intermetallic TiB phase by an in situ chemical reaction [6]. The previous papers have reported that the volume fraction and the distribution of the TiB phase in Ti alloys play a significant role in the improvement of the strength at room and elevated temperatures [4,7–9]. As is known to all that the density of TiB is comparable with that of Ti, and the stiffness is about five times higher than that of Ti. Therefore, the TiB phase provides significant increase in strength and stiffness without increasing the density. In addition, TiB is both thermomechanically stable and essentially insoluble in Ti at all temperatures in the solid state. Moreover, TiB has excellent crystallographic compatibility with Ti, which provides atomically sharp interfaces and chemical compatibility. The coefficient of

thermal expansion of TiB is comparable with that of Ti, which avoids residual stresses at the interfaces during the cooling process [10–12]. As described above, the TiB phase offers unique and wide prospect of application. It is necessary to investigate the formation mechanism of TiB and the interfacial structure of TiB/Ti matrix during the synthesis processing.

Several studies have been focused on this aspect with particular attention on the manufacturing of TiB by different processing routes, including common casting [13,14], powder metallurgy [15], mechanical alloying [16], self-propagation high-temperature synthesis (SHS) [17], spark plasma sintering (SPS) [18,19], and rapid solidification method [20]. Among these techniques, the casting technique was used widely due to its effectiveness and simplicity. For example, it was reported that Ti–6Al–4V [12], Timetal 21S [21], Ti-6242 [22], and Timetal 685 [23] alloys with minor addition of B were successfully prepared by casting and evaluated by the microstructure observation and mechanical properties testing. However, very little information is available in literature on B-modified as-cast high temperature Ti alloys, and no systematic study on the evolution of the TiB phase in the cast alloy is reported. Thus, it would be interesting to know the effect of minor addition of B on high temperature Ti alloys in the as-cast condition.

In present work, the TiB phase was in situ synthesized in the Ti-1100–0.10B alloy by a vacuum induction-melting (VIM) technology. The characteristic of TiB and interfacial structure of TiB/Ti matrix in the alloys were studied. The purpose of this work is to investigate the morphologies of TiB and the TiB/Ti matrix interfaces to explore the formation mechanism of in situ TiB phase in Ti-1100–0.10B alloy.

## 2 Experimental

Sponge Ti (99.80%, mass fraction), high purity Al (99.99%, mass fraction), pure Sn (99.90%, mass fraction), sponge Zr (99.40%, mass fraction), pure Mo (99.95%, mass fraction), pure Si (99.50%, mass fraction) and pure B powder (99.50%, mass fraction) were used as raw materials. The Ti-1100–0.10B alloy was prepared in a VIM furnace. In order to improve the efficiency of melting and reduce the evaporation, the above mentioned materials were compressed into blocks by a pressing equipment before the melting process. The melting stocks weighing 4 kg were melted in a sealed chamber, where a controlled atmosphere of dry high purity argon (99.999%) was maintained at 1000 Pa. Before heating, the chamber was evacuated up to  $10^{-2}$  Pa and backfilled with argon three times in order to minimize the oxygen content. After the raw materials were completely melted, the temperature measurements were carried out by the type C (W–5Re/W–26Re) immersion thermocouple with a Mo–Al<sub>2</sub>O<sub>3</sub> protection and the melt was kept at 1973 K for 2 min. Finally, the alloy melt was poured into a graphite mould and the solidified sample was obtained with a thickness of 12 mm. The chemical compositions of the cast alloy measured by fluorescent spectrometer technique are given in Table 1, and the main chemical compositions were closely controlled to the nominal value.

**Table 1** Chemical compositions of cast alloy

Item	Mass fraction/%						
	Al	Sn	Zr	Mo	Si	B	Ti
Nominal	6.0	2.7	4.0	0.40	0.45	0.10	Bal.
Actual	6.1	2.6	3.8	0.38	0.44	0.09	Bal.

The microstructures were characterized by an Olympus optical microscope (OM), an FEI Quanta 200F scanning electron microscope (SEM) and an FEI Tecnai G<sup>2</sup> F30 transmission electron microscope (TEM). The phase identification of the as-cast sample was conducted by X-ray diffraction (XRD) using a Rigaku D/max–RB X-ray diffractometer with monochromatic Cu K<sub>α</sub> radiation. The samples for OM and SEM observations were prepared according to conventional metallographic

techniques. The samples were polished and etched with Kroll's reagent (10% HNO<sub>3</sub> + 5% HF + 85% H<sub>2</sub>O, volume fraction). The samples for TEM and HRTEM observations were thinned to 50 μm by grinding with SiC sand paper and were punched to discs with 3 mm in diameter. The final stage of thinning was performed by argon ion milling with an incident angle of 10° until perforation occurred.

## 3 Results and discussion

### 3.1 Phase identification and microstructure

The chemical reaction between Ti and B takes place when there exists excess Ti as follows:



Due to the negative Gibbs free energy and reaction formation enthalpy, the reaction is favorable to occur [24]. The XRD spectrum of the as-cast alloy is shown in Fig. 1. It can be observed that the present phases are  $\alpha$ -Ti and TiB, and no peaks of TiB<sub>2</sub> or B are detected. The XRD analysis proves that only TiB can be synthesized by in situ technique, and the reaction of Ti and B is complete. Similar results were reported by CHEN and BOEHLERT [25] in the Ti–6Al–4V–xB alloy.

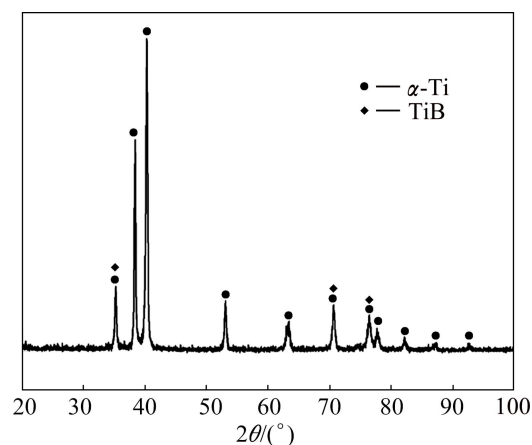


**Fig. 1** XRD pattern of Ti-1100–0.10B alloy in as-cast condition

The representative microstructure of the Ti-1100–0.10B alloy is shown in Fig. 2. It shows Widmanstätten structure with alternative lamellas of  $\alpha$  and  $\beta$  oriented along the particular directions within individual colonies. Such colonies are again distributed within the prior  $\beta$  grains. The prior  $\beta$  grain boundaries in this alloy are decorated by many closely spaced TiB phase with high aspect ratio (needle-like morphology) which forms necklace-type arrangement as shown in Fig. 2(a). The TiB phase is needle-like shape and uniformly dispersed in the Ti matrix as shown in Figs. 2(b) and (c). Figure 2(d) presents a typical SEM morphology of TiB that is

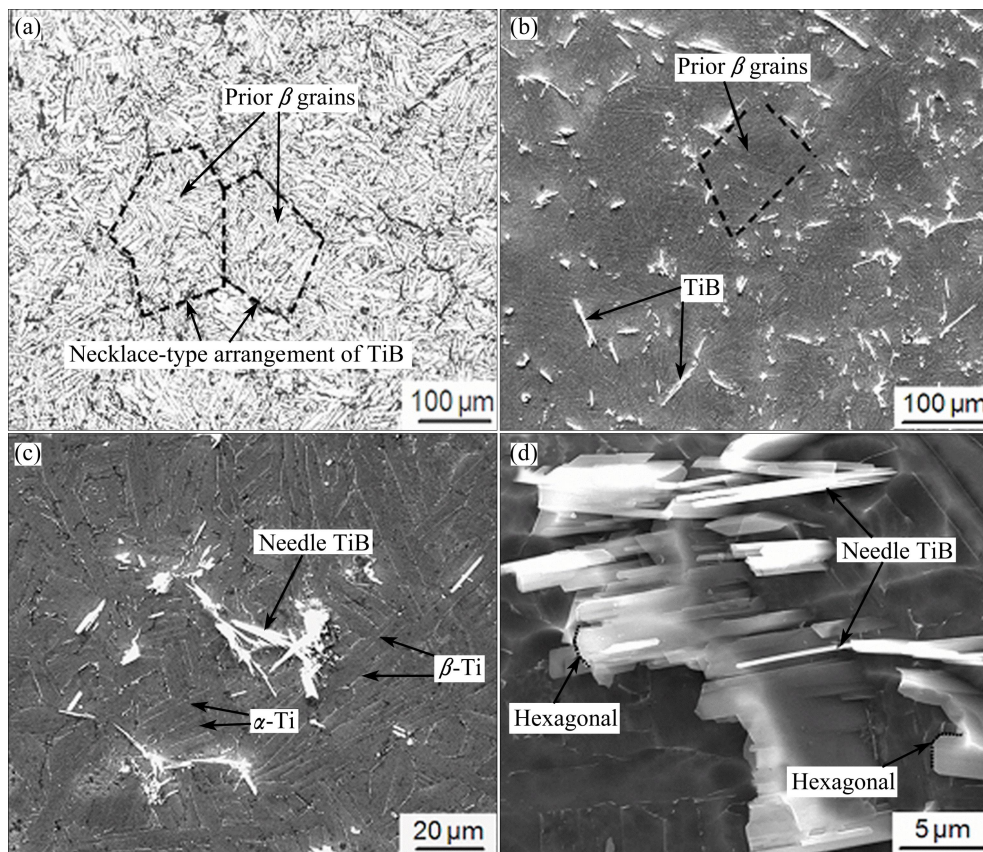


Fig. 2 OM (a–c) and SEM (d) images of Ti-1100–0.10B alloy in as-cast condition

deeply etched. The TiB phase displays needle-like structure with hexagonal transverse cross-sections. Moreover, the interfaces between the TiB phase and the Ti matrix are flat and clean.

B is completely soluble in the liquid phase of Ti (high temperature BCC  $\beta$ ), but is essentially insoluble in the solid Ti phase (room temperature HCP  $\alpha$ ). An appropriate section of the Ti–B phase diagram [11] is shown in Fig. 3 (the present composition is marked by the double arrow). In Ti alloys with hypo-eutectic B concentrations, solidification occurs by the formation of primary  $\beta$ -Ti grains, followed by solidification of a eutectic mixture of  $\beta$ -Ti and TiB phase in the interdendritic regions among the primary  $\beta$ -Ti grains (as demonstrated in Fig. 2). Figure 4 sketches the possible processes emerged during solidification with the addition of B element. If the B content is very low, the B solute rejected at the solidification front can be dispersed readily into the remaining melt, as shown schematically in Fig. 4(a). In this case, TiB will not form until the liquid in the interdendritic region is saturated sufficiently with B. With a higher concentration of B, more B solute will be rejected into the liquid. The constitutional supercooling ahead of the solidification front could happen. Therefore, both alloy and borides nuclei can

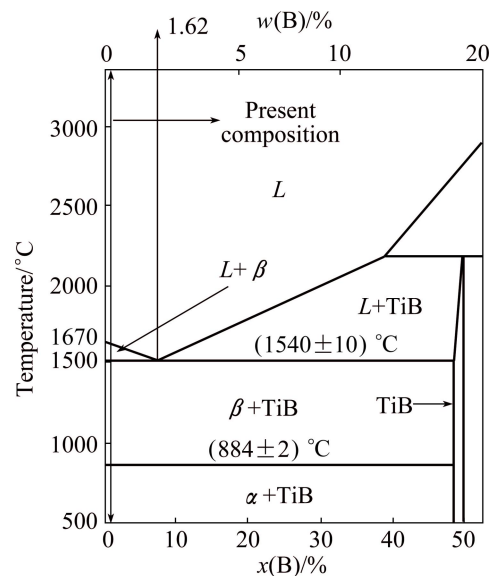


Fig. 3 Section of Ti–B phase diagram

form ahead of the solidification front and the two processes will be inter-related in this situation.

Firstly, the situation that the nucleation of TiB takes place readily is considered, as shown schematically in Fig. 4(b). The formation of TiB will consume B from the liquid phase and reduce the constitutional supercooling. If this is sufficient to preclude the  $\beta$ -Ti formation, the

formation of dendrite will be similar to the situation where the content of B is low (Fig. 4(a)). Secondly, the situation that the  $\beta$ -Ti formation takes place more readily is taken into account, as shown schematically in Fig. 4(c). It is obviously noted that, as new solid alloy forms, the B concentration in the dendritic vicinity will increase further, which inevitably leads to the formation of TiB. The latter process can reduce the B content (and thus the constitutional supercooling) and inhibit the nucleation of the alloy.

The in situ synthesized TiB is prone to nucleate and grow on the lattice-matched planes to minimize the lattice strain existing at the interface between TiB and the Ti matrix [19]. The lattice mismatch between TiB and the Ti matrix has an influence on the crystallographic relationships [26]. The previous investigation suggested

that three types of specific orientation relationships between TiB and  $\beta$ -Ti exist, and can be described as follows [27]:

$$(100)_{\text{TiB}} // (100)_{\beta\text{-Ti}} : [010]_{\text{TiB}} // [010]_{\beta\text{-Ti}} \quad (2)$$

$$(100)_{\text{TiB}} // (110)_{\beta\text{-Ti}} : [010]_{\text{TiB}} // [001]_{\beta\text{-Ti}} \quad (3)$$

$$(100)_{\text{TiB}} // (112)_{\beta\text{-Ti}} : [010]_{\text{TiB}} // [111]_{\beta\text{-Ti}} \quad (4)$$

### 3.2 Formation mechanism of TiB phase

Figure 5(a) shows the bright field TEM image of TiB at longitudinal cross-section. It can be seen that the TiB phase is close to  $\beta$ -Ti phase and extends to the  $\alpha$ -Ti phase matrix in a particular direction. The interface between TiB and Ti matrix is clean, flat and sharp. No interfacial reaction is observed. Figure 5(b) shows the selected area electron diffraction (SAED) pattern of TiB

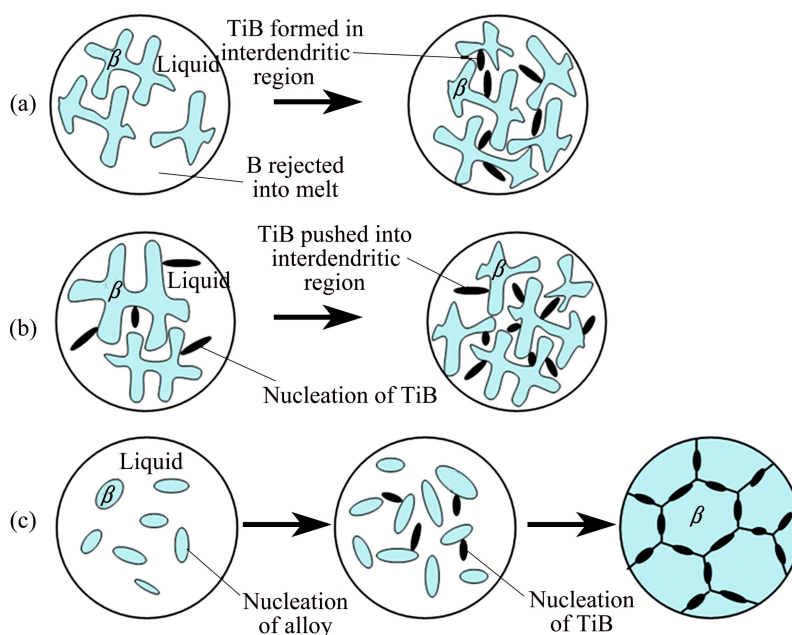


Fig. 4 Schematic views of possible processes during solidification with addition of B

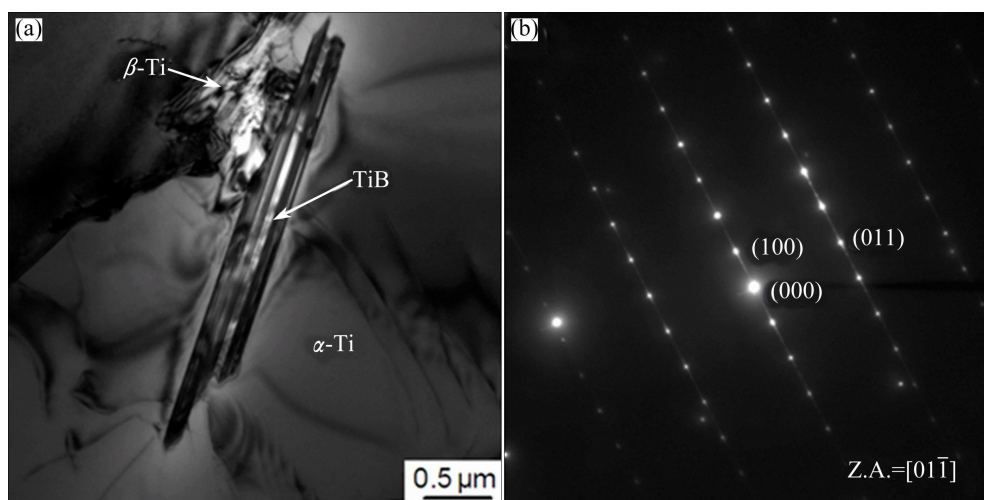


Fig. 5 Bright field TEM image of TiB at longitudinal section (a) and SAED pattern of TiB (b)

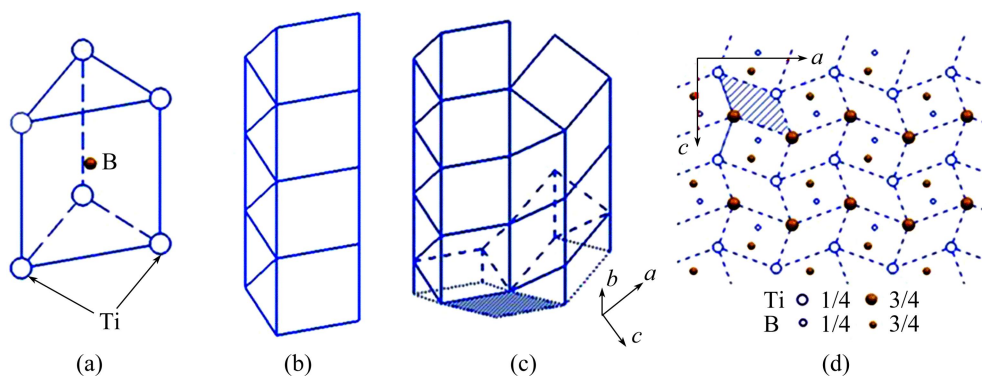
which presents in Fig. 5(a). It reveals that the TiB phase exhibits the B27 orthorhombic structure with the lattice parameters  $a=0.612$  nm,  $b=0.306$  nm, and  $c=0.456$  nm [28–30]. The bright streak occurs on the  $(100)_{\text{TiB}}$  plane, which demonstrates that there are stacking faults in TiB and the plane of stacking faults is  $(100)$ .

The study of the crystal structure of TiB is helpful to get an insight of the morphology of the in situ TiB phase formed during the solidification process. TiB is known to have a B27 structure, consisting of trigonal prisms stacked horizontally in columnar arrays connected only at their edges. It has a zigzag chain of B atoms along the  $[010]$  direction [24,31]. Figure 6 illustrates the atomic packing in TiB. As shown in Fig. 6(a), each B atom lies at the center of a trigonal prism of six Ti atoms. The B27 structure consists of trigonal prisms stacked in columnar arrays sharing only two rectangular planes with neighbouring prisms, and the columns are connected only along their edges, as shown in Figs. 6(b) and (c). B atoms in this manner form a zigzag chain along the B27  $[010]$  direction, and form B-free “pipes” of Ti atoms with a trapezoidal cross-section, as indicated by the shaded area in Fig. 6(c). Figure 6(d) shows the projection of the TiB structure on

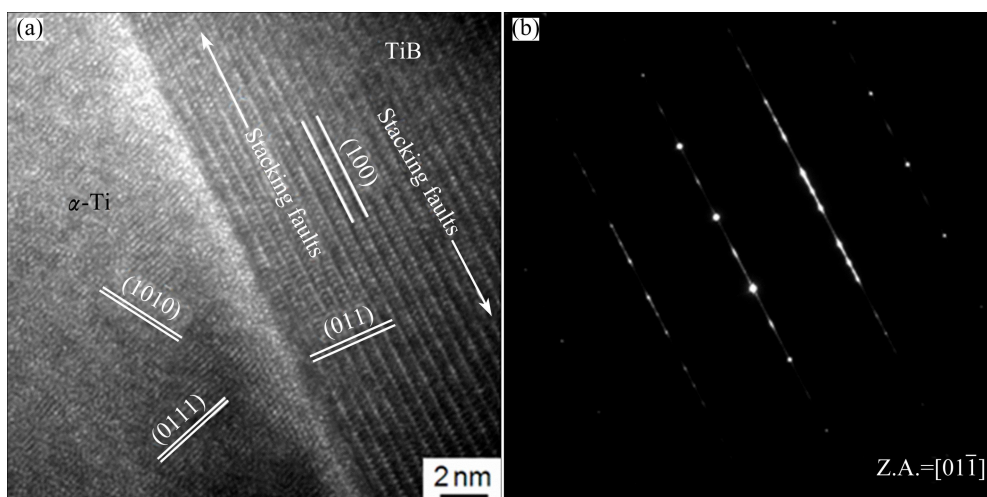
the B27  $(010)$  plane. Based on the above arguments, it is known that Ti and B atoms have the same stoichiometry along the B27  $[010]$  direction. According to the periodic bond chain theory, TiB should exhibit faster growth along the  $[010]$  direction than that of normal along the  $[100]$ ,  $[101]$  and  $[001]$  directions. Since growing crystals are usually restrained by the slowest-growing facets, TiB with the B27 structure should form a needle-like morphology with the needle axis parallel to the  $[010]$  direction, as shown in Fig. 5.

Figure 7(a) shows the interfacial structure between the TiB longitudinal cross-section and the Ti matrix. Lots of stacking faults on the  $(100)_{\text{TiB}}$  plane can be observed. The interface between the TiB and the  $\alpha$ -Ti matrix is clean without any defects, and the TiB phase does not exhibit any specific orientation relationship with the  $\alpha$ -Ti matrix. The streak on the  $(100)_{\text{TiB}}$  plane also indicates that plane faults exist on the  $(100)_{\text{TiB}}$  plane in the in situ synthesized TiB (Fig. 7(b)).

Figure 8(a) shows the HRTEM image of the TiB phase and Fig. 8(b) shows the inverse fast Fourier transformation (FFT) image of the stacking faults in Fig. 8(a). It can be seen that there are high density stacking faults on the  $(100)_{\text{TiB}}$  plane and the space between each



**Fig. 6** Schematic illustrations of crystal structure of TiB: (a) Basic trigonal prismatic arrangement of Ti atoms around each B atom; (b) Columns of prisms; (c) Arrangement of basic trigonal prisms to form TiB structure; (d) Projection of TiB structure on  $(010)$  plane



**Fig. 7** HRTEM image of TiB/ $\alpha$ -Ti interface (a) and SAED pattern of TiB phase (b)

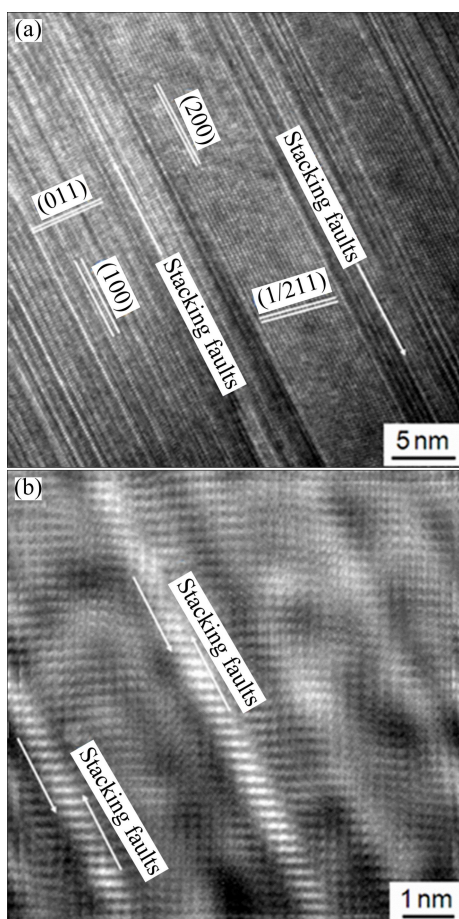


**Fig. 8** HRTEM image of TiB phase (a) and inverse FFT image of stacking faults (b)

stacking fault layer is not equal.

Since the formation of TiB phase can be regarded as a vacancy diffusion process of B atoms in the Ti matrix [14,29,32], the sites of B atoms during the growth process are analyzed to obtain a better understanding of the formation mechanism of the stacking faults. As shown in Fig. 9, the stacking sequence along the  $[100]_{\text{TiB}}$  direction is  $abb'a'ABB'A'$ . The stacking period of atomic planes in  $[010]$  and  $[001]$  directions are  $\alpha\beta\alpha\beta\cdots$  and  $\alpha\alpha'\beta\beta'\alpha\alpha'\beta\beta'\cdots$ , respectively. The stacking sequence along the  $[100]_{\text{TiB}}$  direction is more complex than those along the  $[010]_{\text{TiB}}$  and  $[001]_{\text{TiB}}$  directions. The lack of B atoms is likely to happen because the amount of B atom in the melt is much less than that of Ti atom. Accordingly, it will lead to the formation of stacking faults on the (100) plane when there is a lack of B atoms to occupy the positions of  $a, a', A$  and  $A'$ . Because the formation of stacking faults is due to the consumption of B atoms, namely the B atoms on the sites of  $a, a', A$  and  $A'$  are absent, the stacking faults are intrinsic fault. Moreover, the stacking faults formed on the  $(100)_{\text{TiB}}$  plane have a minimum energy as compared with those formed on the  $(001)_{\text{TiB}}$  and  $(010)_{\text{TiB}}$  planes. Thus, stacking faults form only on the  $(100)_{\text{TiB}}$  plane. The stacking faults in the

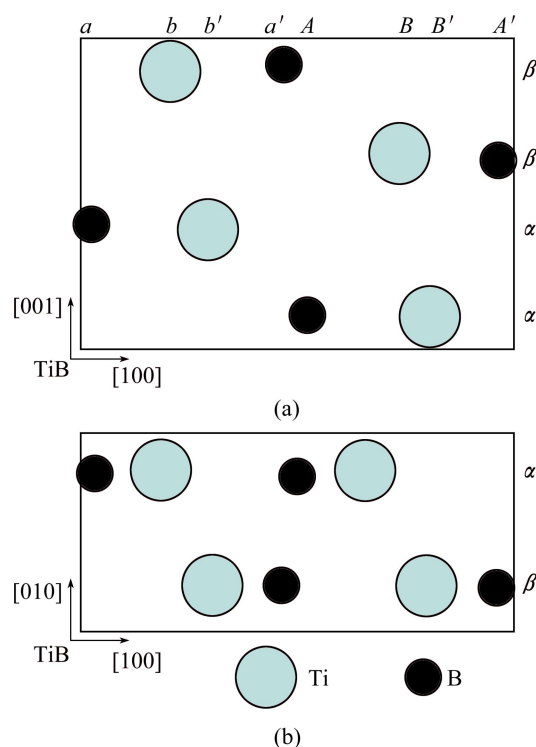


**Fig. 9** Schematic diagrams of atom projection of TiB along  $[010]$  (a) and  $[001]$  (b) directions

(100) plane serve to minimize the lattice strain at the interfaces. The location of B atoms and the lattice mismatch energy between TiB and Ti matrix play a key role in the formation of stacking faults during the growth process of TiB phase.

## 4 Conclusions

1) The microstructures of the Ti-1100–0.10B alloy consist of  $\alpha$ -Ti,  $\beta$ -Ti as well as eutectic TiB phase, and the TiB phase prefers to precipitating at the prior  $\beta$  grain boundaries.

2) The precipitation pathways of the TiB phase are obtained as follows:

Liquid  $\rightarrow$  Liquid + primary  $\beta$   $\rightarrow$  Eutectic (TiB +  $\beta$ )

3) The TiB phase is readily to grow along the  $[010]$  direction with the morphology of needle-like shape. The transverse cross-section of the TiB phase shows a hexagonal shape. The interfaces between TiB and Ti matrix are clean and devoid of any defects. The formation of above morphologies serves to minimize the lattice strain at the interfaces.

4) There are lots of stacking faults in the TiB phase, which are likely to form on the (100) plane of TiB. The crystal structure (B27) of TiB and the lattice mismatch energy between TiB and Ti matrix are the mechanisms of the formation of stacking faults during the growth process of the TiB phase.

## References

- [1] ZHANG A-li, LIU Dong, TANG Hai-bo, WANG Hua-ming. Microstructure evolution of laser deposited Ti60A titanium alloy during cyclic thermal exposure [J]. Transactions of Nonferrous Metals Society of China, 2013, 23(11): 3249–3256.
- [2] PRASAD K, SARKAR R, KAMAT S V, NANDY T K. Tensile behaviour of boron modified Timetal 834 titanium alloy in the intermediate temperature range 400–500 °C [J]. J Alloys Compd, 2011, 509: 7361–7367.
- [3] ZHAO Er-tuan, KONG Fan-tao, CHEN Yu-yong, LI Bao-hui. Interfacial reactions between Ti-1100 alloy and ceramic mould during investment casting [J]. Transactions of Nonferrous Metals Society of China, 2011, 21(S2): s348–s352.
- [4] PRASAD K, SARKAR R, GHOSAL P, SATYANARAYANA D V V, KAMAT S V, NANDY T K. Tensile and creep properties of thermomechanically processed boron modified Timetal 834 titanium alloy [J]. Mater Sci Eng A, 2011, 528(22–23): 6733–6741.
- [5] CHEN W, BOEHLERT C J. The 455 °C tensile and fatigue behavior of boron modified Ti–6Al–2Sn–4Zr–2Mo–0.1Si (wt.%) [J]. Int J Fatigue, 2010, 32(5): 799–807.
- [6] FENG H B, JIA D C, ZHOU Y, HUO J. Microstructural characterisation of in situ TiB/Ti matrix composites prepared by mechanical alloying and hot pressing [J]. Mater Sci Technol, 2004, 20(9): 1205–1210.
- [7] ZHANG Zhao-hui, SHEN Xiang-bo, WANG Fu-chi, WEI Sai, LI Shu-kui, CAI hong-nian. Microstructure characteristics and mechanical properties of TiB/Ti–1.5Fe–2.25Mo composites synthesized in situ using SPS process [J]. Transactions of Nonferrous Metals Society of China, 2013, 23(9): 2598–2604.
- [8] HUANG Lu-jun, CUI Xi-ping, GENG Lin, FU Yu. Effects of rolling deformation on microstructure and mechanical properties of network structured TiB<sub>w</sub>/Ti composites [J]. Transactions of Nonferrous Metals Society of China, 2012, 22(S1): s79–s83.
- [9] LIU B X, HUANG L J, GENG L, WANG B, CUI X P. Effects of reinforcement volume fraction on tensile behaviors of laminated Ti–TiB<sub>w</sub>/Ti composites [J]. Mater Sci Eng A, 2014, 610: 344–349.
- [10] IVASISHIN O M, TELIOVYCH R V, IVANCHENKO V G, TAMIRISAKANDALA S, MIRACLE D B. Processing, microstructure, texture, and tensile properties of the Ti–6Al–4V–1.55B eutectic alloy [J]. Metall Mater Trans A, 2008, 39(2): 402–416.
- [11] SRINIVASAN R, MIRACLE D, TAMIRISAKANDALA S. Direct rolling of as-cast Ti–6Al–4V modified with trace additions of boron [J]. Mater Sci Eng A, 2008, 487(1): 541–551.
- [12] SEN I, TAMIRISAKANDALA S, MIRACLE D B, RAMAMURTY U. Microstructural effects on the mechanical behavior of B-modified Ti–6Al–4V alloys [J]. Acta Mater, 2007, 55(15): 4983–4993.
- [13] GUO Xiang-long, WANG Li-qiang, QIN Ji-ning, LÜ Wei-jie, ZHANG Di. Microstructure and mechanical properties of (TiB+La<sub>2</sub>O<sub>3</sub>)/Ti composites heat treated at different temperatures [J]. Transactions of Nonferrous Metals Society of China, 2014, 24(6): 1737–1743.
- [14] LU W J, ZHANG D, ZHANG X N, WU R J, SAKATA T, MORI H. Microstructural characterization of TiB in in situ synthesized titanium matrix composites prepared by common casting technique [J]. J Alloys Compd, 2001, 327(1–2): 240–247.
- [15] ZHANG Yu-zi, HUANG Lu-jun, LIU Bao-xi, GENG Lin. Hot deformation behavior of in-situ TiB<sub>w</sub>/Ti6Al4V composite with novel network reinforcement distribution [J]. Transactions of Nonferrous Metals Society of China, 2012, 22(S2): s465–s471.
- [16] GODFREY T M T, WISBEY A, GOODWIN P S, BAGNALL K, WARD-CLOSE C M. Microstructure and tensile properties of mechanically alloyed Ti–6Al–4V with boron additions [J]. Mater Sci Eng A, 2000, 282(1): 240–250.
- [17] ZHANG X H, XU Q, HAN J C, KVANNIN V L. Self-propagating high temperature combustion synthesis of TiB/Ti composites [J]. Mater Sci Eng A, 2003, 348(1–2): 41–46.
- [18] FENG H B, ZHOU Y, JIA D C, MENG Q C. Microstructure and mechanical properties of in situ TiB reinforced titanium matrix composites based on Ti–FeMo–B prepared by spark plasma sintering [J]. Compos Sci Technol, 2004, 64(16): 2495–2500.
- [19] FENG H B, ZHOU Y, JIA D C, MENG Q C. Microstructural characterization of spark plasma sintered in situ TiB reinforced Ti matrix composite by EBSD and TEM [J]. Mater Trans, 2005, 46(3): 575–580.
- [20] TJONG S C, MAI Y W. Processing-structure-property aspects of particulate- and whisker-reinforced titanium matrix composites [J]. Compos Sci Technol, 2008, 68(3–4): 583–601.
- [21] CHERUKURI B, SRINIVASAN R, TAMIRISAKANDALA S, MIRACLE D B. The influence of trace boron addition on grain growth kinetics of the beta phase in the beta titanium alloy Ti–15Mo–2.6Nb–3Al–0.2Si [J]. Scripta Mater, 2009, 60(7): 496–499.
- [22] LU W J, ZHANG D, ZHANG X N, WU R J, SAKATA T, MORI H. Microstructure and tensile properties of in situ (TiB+TiC)/Ti6242 (TiB:TiC=1:1) composites prepared by common casting technique [J]. Mater Sci Eng A, 2001, 311(1): 142–150.
- [23] CHANDRAVANSHI V K, SARKAR R, GHOSAL P, KAMAT S V, NANDY T K. Effect of minor additions of boron on microstructure and mechanical properties of as-cast near  $\alpha$  titanium alloy [J]. Metall Mater Trans A, 2010, 41(4): 936–946.
- [24] FENG H B, ZHOU Y, JIA D C, MENG Q C. Rapid synthesis of Ti alloy with B addition by spark plasma sintering [J]. Mater Sci Eng A, 2005, 390(1–2): 344–349.
- [25] CHEN W, BOEHLERT C J. Texture induced anisotropy in extruded Ti–6Al–4V–xB alloys [J]. Mater Charact, 2011, 62(3): 333–339.
- [26] LU W J, ZHANG D, ZHANG X N, WU R J, SAKATA T, MORI H. HREM study of TiB/Ti interfaces in a Ti–TiB–TiC in situ composite [J]. Scripta Mater, 2001, 44(7): 1069–1075.
- [27] PANDA K B, CHANDRAN K S R. Synthesis of ductile titanium–titanium boride (Ti–TiB) composites with a beta-titanium matrix: The nature of TiB formation and composite properties [J]. Metall Mater Trans A, 2003, 34(6): 1371–1385.
- [28] GRAEF M D E, LÖFVANDER J P A, MCCULLOUGH C, LEVI C G. The evolution of metastable B<sub>f</sub> borides in a Ti–Al–B alloy [J]. Acta Metal Mater, 1992, 40(12): 3395–3406.
- [29] FENG H B, ZHOU Y, JIA D C, MENG Q C, RAO J C. Growth mechanism of in situ TiB whiskers in spark plasma sintered TiB/Ti metal matrix composites [J]. Cryst Growth Des, 2006, 6(7): 1626–1630.
- [30] HYMAN M E, MCCULLOUGH C, VALENCLA J J, LEVI C G, MEHRABLAN R. Microstructure evolution in TiAl alloys with B additions: Conventional solidification [J]. Metall Mater Trans A, 1989, 20(9): 1847–1859.
- [31] LU W J, XIAO L, GENG K, QIN J N, ZHANG D. Growth mechanism of in situ synthesized TiB<sub>w</sub> in titanium matrix composites prepared by common casting technique [J]. Mater Charact, 2008, 59(7): 912–919.
- [32] FENG H B, ZHOU Y, JIA D C, MENG Q C. Stacking faults formation mechanism of in situ synthesized TiB whiskers [J]. Scripta Mater, 2006, 55(8): 667–670.

## 铸造 Ti-1100–0.10B 合金中 原位合成 TiB 相的显微组织表征

付彬国, 王宏伟, 邹鹤鸣, 魏尊杰

哈尔滨工业大学 金属精密热加工国家级重点实验室, 哈尔滨 150001

**摘 要:** 采用真空感应熔炼技术制备 Ti-1100–0.10B 合金, 并对原位合成 TiB 相的显微组织特征以及 TiB 相与 Ti 基体的界面结构进行系统研究。结果表明: TiB 相优先在原始  $\beta$  晶界处析出。TiB 相沿[010]方向择优生长形成典型的针状形貌, 横断面为六角结构。TiB 相与 Ti 基体的界面非常干净, 没有析出相出现。TiB 相内部的(100)面上出现大量的堆垛层错, 这归因于 B 原子在 TiB 晶体结构中的位置以及 TiB 与 Ti 基体的晶格错配能。

**关键词:** 钛合金; 铸造; 显微组织; TiB

(Edited by Mu-lan QIN)